

Global organization of neuronal activity only requires unstructured local connectivity

March 11, 2021

David Dahmen,^{1*†} Moritz Layer,^{1,2*} Lukas Deutz,^{1,3} Paulina Anna Dąbrowska,^{1,2} Nicole Voges,^{1,4} Michael von Papen,¹ Thomas Brochier,⁴ Alexa Riehle,^{1,4} Markus Diesmann,^{1,5,6} Sonja Grün,^{1,7} Moritz Helias^{1,5}

¹Institute of Neuroscience and Medicine (INM-6) and Institute for Advanced Simulation (IAS-6) and JARA Institut Brain Structure-Function Relationships (INM-10), Jülich Research Centre, Jülich, Germany

²RWTH Aachen University, Aachen, Germany

³School of Computing, University of Leeds, Leeds, West Yorkshire, United Kingdom

⁴Institut de Neurosciences de la Timone (INT), CNRS - Aix-Marseille University, Marseille, France

⁵Department of Physics, Faculty 1, RWTH Aachen University, Aachen, Germany

⁶Department of Psychiatry, Psychotherapy and Psychosomatics, School of Medicine, RWTH Aachen University, Aachen, Germany

⁷Theoretical Systems Neurobiology, RWTH Aachen University, Aachen, Germany

*Equal contribution

†To whom correspondence should be addressed; E-mail: d.dahmen@fz-juelich.de.

Modern electrophysiological recordings simultaneously capture single-unit spiking activities of hundreds of neurons spread across large cortical distances. Yet this massively parallel activity is often confined to relatively low-dimensional manifolds. This implies strong coordination also among neurons that are most likely not even connected. Here, we combine in vivo recordings with network models and theory to characterize the nature of mesoscopic coordination patterns in macaque motor cortex and to expose their origin: We find that heterogeneity in local connectivity supports network states with complex long-range cooperation between neurons that arises from multi-synaptic, short-range connections. Our theory explains the experimentally observed spatial organization of covariances in resting state recordings as well as the behaviorally related modulation of covariance patterns during a reach-to-grasp task. The ubiquity of heterogeneity in local cortical circuits suggests that the brain uses the described mechanism to flexibly adapt neuronal coordination to momentary demands.

Introduction

Complex brain functions require coordination between large numbers of neurons. Unraveling mechanisms of neuronal coordination is therefore a core ingredient towards answering the long-standing question of how neuronal activity represents information. Population coding is one classical paradigm (1) in which entire populations of neurons behave coherently, thus leading to positive correlations among their members. The emergence and dynamical control of such population-averaged correlations has been studied intensely (2, 3, 4, 5). More recently, evidence accumulated that neuronal activity evolves within manifolds, which implies even more involved ways of

39 neuronal activity coordination (6, 7, 8): A small number of population-wide activity patterns, the neural modes, are
40 thought to explain most variability of neuronal activity. In this case, individual neurons do not necessarily follow a
41 stereotypical activity pattern that is identical across all neurons contributing to a representation. Instead the coord-
42 ination among the members is determined by more complex relations. Simulations of recurrent network models
43 indeed indicate that networks trained to perform a realistic task exhibit activity organized in manifolds (9). The
44 dimensionality of such manifolds is determined by the structure of correlations (10, 11) and tightly linked to the
45 complexity of the task the network has to perform (12) as well as to the dimensionality of the stimulus (13). Recent
46 work has started to decipher how neural modes and the dimensionality of activity are shaped by features of network
47 connectivity, such as heterogeneity of connections (14), block structure (15, 16), and low-rank perturbations (17) of
48 connectivity matrices, as well as connectivity motifs (18, 19). Yet, these works neglected the spatial organization of
49 network connectivity (20) that becomes more and more important with current experimental techniques that allow
50 the simultaneous recording of ever more neurons. How distant neurons that are likely not connected can still be
51 strongly coordinated to participate in the same neural mode is a widely open question.

52 To answer this question, we combine analysis of massively parallel spiking data from macaque motor cortex
53 with the analytical investigation of a spatially organized neuronal network model. We here quantify coordina-
54 tion by pairwise covariances, which measure how temporal departures of the neurons' activities away from their
55 mean firing rate are correlated. We show that, even with only unstructured and short-range connections, strong
56 covariances across distances of several millimeters emerge naturally in balanced networks if their dynamical state
57 is close to an instability within a "critical regime". While mean covariances are readily accessible by mean-field
58 techniques and have been shown to be small in balanced networks (3, 21), explaining covariances on the level of in-
59 dividual pairs requires methods from statistical physics of disordered systems. With such a theory, here derived for
60 spatially organized excitatory-inhibitory networks, we show that large individual covariances arise at all distances
61 if the network is close to the critical point. These predictions are confirmed by recordings of macaque motor cortex
62 activity. The long-range coordination found in this study is not merely determined by the anatomical connectivity,
63 but depends substantially on the network state, which is characterized by the individual neurons' mean firing rates.
64 This allows the network to adjust the neuronal coordination pattern in a dynamic fashion, which we demonstrate
65 through simulations and by comparing two behavioral epochs of a reach-to-grasp experiment.

67 Results

68 Macaque motor cortex shows long-range coordination patterns

69 We first analyze data from motor cortex of macaques during rest, recorded with $4 \times 4 \text{ mm}^2$, 100-electrode Utah
70 arrays with $400 \mu\text{m}$ inter-electrode distance (Figure 1A). The resting condition of motor cortex in monkeys is
71 ideal to assess intrinsic coordination between neurons during ongoing activity. In particular, our analyses focus
72 on true resting state data, devoid of movement-related transients in neuronal firing (see Methods). Massively-
73 parallel single-unit spiking activity of ≈ 130 neurons per recording session, sorted into putative excitatory and
74 inhibitory cells, shows strong spike-count covariances across the entire Utah array, well beyond the typical scale
75 of the underlying short-range connectivity profiles (Figure 1B,D). Positive and negative covariances form patterns
76 in space that are furthermore seemingly unrelated to the neuron types. All populations show a large dispersion
77 of both positive and negative covariance values (Figure 1C). Given the classical view on pairwise covariances in
78 balanced networks (2, 22, 23, 21, 4), this result comes unexpected: A common finding is that covariances averaged
79 across many pairs of cells are small if the network dynamics is stabilized by an excess of inhibitory feedback;
80 dynamics known as the 'balanced state' arise (24, 25, 26): Negative feedback counteracts any coherent increase
81 or decrease of the population-averaged activity, preventing the neurons from fluctuating in unison (21). Breaking
82 this balance in different ways leads to large covariances (5, 27, 28). Can the observation of significant covariances
83 between individual cells across large distances be reconciled with the balanced state? In the following, we provide
84 a mechanistic explanation.

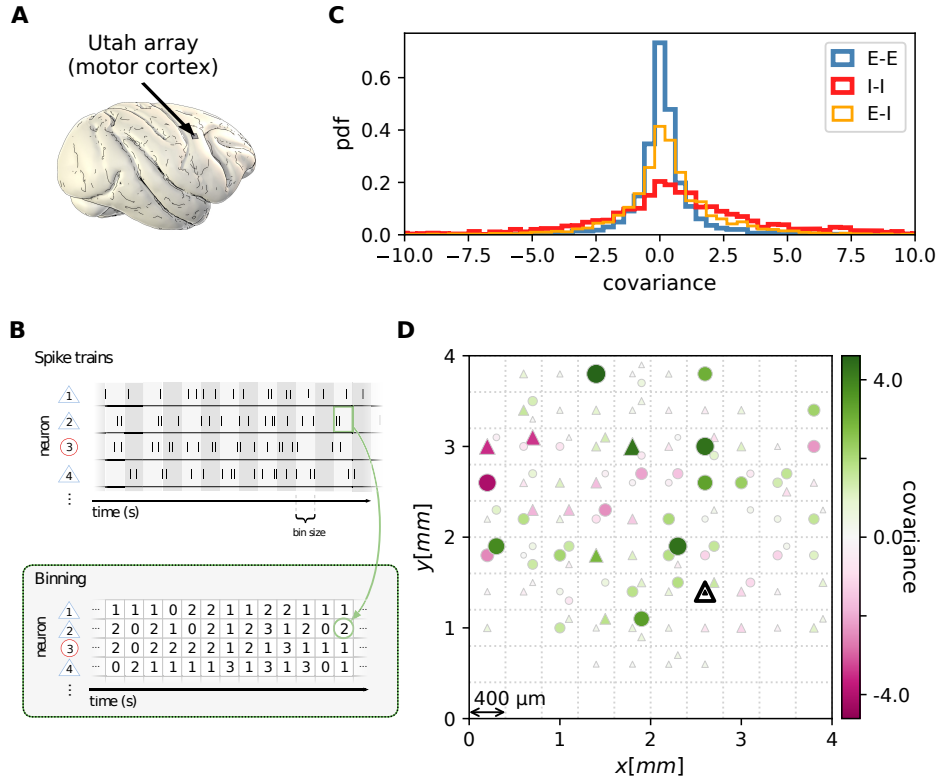


Figure 1: Salt-and-pepper structure of covariances in motor cortex. (A) Sketch of 10×10 Utah electrode array recording in motor cortex of macaque monkey during rest. (B) Spikes are sorted into putative excitatory (blue triangles) and inhibitory (red circles) single units according to widths of spike waveforms (see supplement). Resulting spike trains are binned in 1 s bins to obtain spike counts. (C) Population-resolved distribution of pairwise spike-count covariances in session E2 (E-E: excitatory-excitatory, E-I: excitatory-inhibitory, I-I: inhibitory-inhibitory). (D) Pairwise spike-count covariances with respect to the neuron marked by black triangle in one recording (session E2, see Methods). Grid indicates electrodes of a Utah array, triangles and circles correspond to putative excitatory and inhibitory neurons, respectively. Size as well as color of markers represent covariance. Neurons within the same square were recorded on the same electrode.

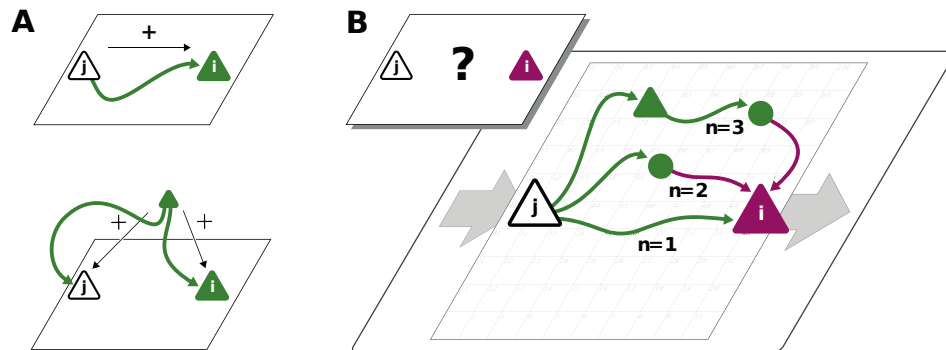


Figure 2: **Covariances from direct and indirect connections.** (A) Positive covariance (green neuron i) follows from direct excitatory connection (top) or shared input (middle). (B) Negative covariance (magenta) between two excitatory neurons cannot be explained by direct connections: Neuronal interactions are not only mediated via direct connections ($n = 1$; sign uniquely determined by presynaptic neuron type) but also via indirect paths of different length $n > 1$. The latter may have any sign (positive: green; negative: purple) due to intermediate neurons of arbitrary type (triangle: excitatory, circle: inhibitory).

85 Multi-synaptic connections determine covariances

86 Connections mediate interactions between neurons. Many studies therefore directly relate connectivity and covariances (22, 23, 29, 30, 31). From direct connectivity, one would expect positive covariances between excitatory neurons and negative covariances between inhibitory neurons and a mix of negative and positive covariances only for excitatory-inhibitory pairs. Likewise, a shared input from inside or outside the network only imposes positive covariances between any two neurons (Figure 2A). The observations that excitatory neurons may have negative covariances (Figure 1D), as well as the broad distribution of covariances covering both positive and negative values (Figure 1C), are not compatible with this view. In fact, the sign of covariances appears to be independent of the neuron types. So how do negative covariances between excitatory neurons arise?

94 The view that equates connectivity with correlation implicitly assumes that the effect of a single synapse on the receiving neuron is weak. This view, however, regards each synapse in isolation. Could there be states in the network where, collectively, many weak synapses cooperate, as perhaps required to form neuronal manifolds? In such a state, interactions may not only be mediated via direct connections but also via indirect paths through the network (Figure 2B). Such effective multi-synaptic connections may explain our observation that far apart neurons that are basically unconnected display considerable correlation of arbitrary sign.

100 Let us here illustrate the ideas first and corroborate them in subsequent sections. Direct connections yield covariances of a predefined sign, leading to covariance distributions with multiple peaks, e.g. a positive peak for excitatory neurons that are connected and a peak at zero for neurons that are not connected. Multi-synaptic paths, however, involve both excitatory and inhibitory intermediate neurons, which contribute to the interaction with different signs (Figure 2B). Hence, a single indirect path can contribute to the total interaction with arbitrary sign (22). If indirect paths dominate the interaction between two neurons, the sign of the resulting covariance becomes independent of their type. Given that the connecting paths in the network are different for any two neurons, the resulting covariances can fall in a wide range of both positive and negative values, giving rise to the broad distributions for all combinations of neuron types in Figure 1C. This provides a hypothesis why there may be no qualitative difference between the distribution of covariances for excitatory and inhibitory neurons. In fact, their widths are similar and their mean is close to zero (see Methods for exact values); the latter being the hallmark of the negative feedback that characterizes the balanced state. The subsequent model-based analysis will substantiate

112 this idea and show that it also holds for networks with spatially organized heterogeneous connectivity.

113 To play this hypothesis further, an important consequence of the dominance of multi-synaptic connections
114 could be that covariances are not restricted to the spatial range of direct connectivity. Through interactions via
115 indirect paths the reach of a single neuron could effectively be increased. But the details of the spatial profile of the
116 covariances in principle could be highly complex as it depends on the interplay of two antagonistic effects: On the
117 one hand, signal propagation becomes weaker with distance, as the signal has to pass several synaptic connections.
118 Along these paths mean firing rates of neurons are typically diverse, and so are their signal transmission properties
119 (32). On the other hand, the number of contributing indirect paths between any pair of neurons proliferates with
120 their distance. With single neurons typically projecting to thousands of other neurons in cortex, this leads to
121 involved combinatorics; intuition here ceases to provide a sensible hypothesis on what is the effective spatial
122 profile and range of coordination between neurons. Also it is unclear which parameters these coordination patterns
123 depend on. The model-driven and analytical approach of the next section will provide such a hypothesis.

124 **Networks close to instability show shallow exponential decay of covariances**

125 To gain an understanding of the spatial features of intrinsically generated covariances in balanced critical networks,
126 we model a network of excitatory and inhibitory neurons on a two-dimensional sheet (Figure 3A, for details see
127 Methods). The probability of two neurons being connected decays with distance on a characteristic length scale
128 d . Previous studies have used linear response theory in combination with methods from statistical physics and
129 field theory to gain analytic insights into both mean covariances (2, 33, 22, 21) and the width of the distribution of
130 covariances (14). Field-theoretic approaches thereby were, however, restricted to purely random networks devoid
131 of any network structure and thus not suitable to study spatial features of covariances. To analytically quantify the
132 relation between the spatial ranges of covariances and connections, we therefore here develop a theory for spatially
133 organized random networks with multiple populations. The model captures the predominant type of heterogeneity
134 in cortical networks, namely the sparseness of connections.

135 A distance-resolved histogram of the covariances in the spatially organized E-I network shows that the mean
136 covariance is close to zero but the width or variance of the covariance distribution stays large, even for large
137 distances (Figure 3C). Analytically, we derive that, despite the complexity of the various indirect interactions, both
138 the mean and the variance of covariances follow simple exponential laws in the long-distance limit (see supplement
139 S3- S11). These laws are universal in that they do not depend on details of the spatial profile of connections. Our
140 theory shows that the associated length scales are strikingly different for means and variances of covariances.
141 They each depend on the reach of direct connections and on specific eigenvalues of the effective connectivity
142 matrix. These eigenvalues summarize various aspects of network connectivity and signal transmission into a
143 single number: Each eigenvalue belongs to a “mode”, a combination of neurons that act collaboratively, rather
144 than independently, coordinating neuronal activity within a one-dimensional subspace. To start with, there are as
145 many such subspaces as there are neurons. But if the spectral bound in Figure 3B is close to one, only a relatively
146 small fraction of them, namely those close to the spectral bound, dominate the dynamics; the dynamics is then
147 effectively low-dimensional and multi-synaptic connections may become effective.

148 To quantify this idea, for the mean covariance \bar{c} we find that the dominant behavior is an exponential decay
149 $\bar{c} \sim \exp(-x/\bar{d})$ on a length scale \bar{d} that is determined by the population eigenvalue (Figure 3B). Its position
150 depends on the ratio between excitation and inhibition in the network and becomes more negative in more strongly
151 inhibition-dominated networks. We show in supplement S8.4 that this leads to a steep decay of mean covariances
152 with distance. The variance of covariances, however, predominantly decays exponentially on a length scale d_{eff}
153 that is determined by the spectral bound R , the largest real part among all eigenvalues (Figure 3B,D). In inhibition-
154 dominated networks, R is determined by the heterogeneity of connections. For $R \lesssim 1$ we obtain the effective
155 length scale

$$\frac{d_{\text{eff}}}{d} \sim \sqrt{\frac{R^2}{1-R^2}} + \text{const.} \gg 1. \quad (1)$$

156 What this means is that precisely at the point where R is close to one, when the low-dimensional manifold forms,

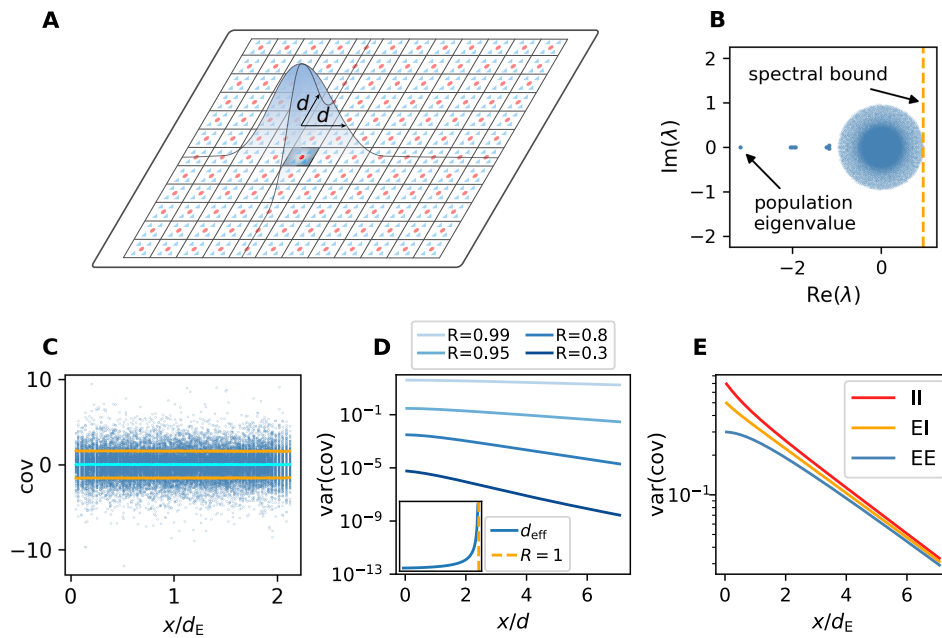


Figure 3: **Spatially organized E-I network model.** (A) Network model: space is divided into cells with four excitatory (triangles) and one inhibitory (circle) neuron each. Distance-dependent connection probabilities (shaded areas) are defined with respect to cell locations. (B) Eigenvalues λ of effective connectivity matrix for network in dynamically balanced critical state. Each dot shows the real part $\text{Re}(\lambda)$ and imaginary part $\text{Im}(\lambda)$ of one complex eigenvalue. The spectral bound (dashed vertical line) denotes the right-most edge of the eigenvalue spectrum. (C) Simulation: covariances of excitatory neurons over distance x between cells (blue dots: individual pairs; cyan: mean; orange: standard deviation; sample of 150 covariances at each of 200 chosen distances). (D) Theory: Variance of covariance distribution as a function of distance x for different spectral bounds of the effective connectivity matrix. *Inset*: effective decay constant of variances diverges as the spectral bound approaches one. (E) For large spectral bounds, the variances of EE, EI, and II covariances decay on a similar length scale. Spectral bound $R = 0.95$. Other parameters see Table T2 in supplement.

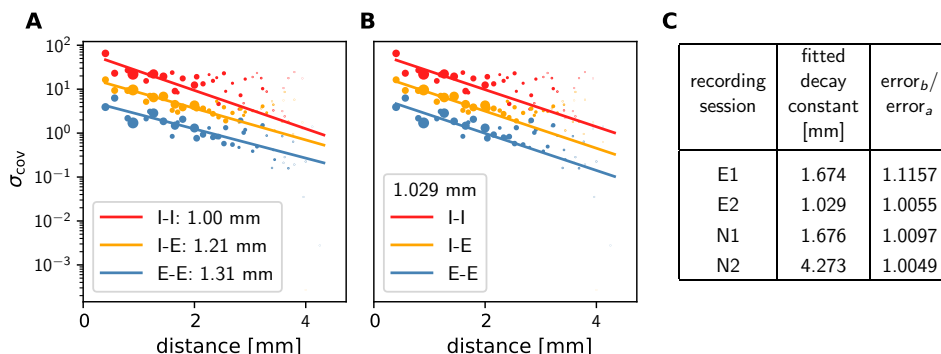


Figure 4: Long-range covariances in macaque motor cortex. Variance of covariances as a function of distance. (A) Population-specific exponential fits (lines) to variances of covariances (dots) in session E2, with fitted decay constants indicated in the legend (I-I: putative inhibitory neuron pairs, I-E: inhibitory-excitatory, E-E: excitatory pairs). Dots show the empirical estimate of the variance of the covariance distribution for each distance. Size of the dots represents relative count of pairs per distance and was used as weighting factor for the fits to compensate for uncertainty at large distances, where variance estimates are based on fewer samples. Mean squared error 2.918. (B) Population-specific exponential fits (lines) analogous to (A), with slopes constrained to be identical. This procedure yields a single fitted decay constant indicated in the legend. Mean squared error 2.934. (C) Table listing decay constants fitted as in (B) for all recording sessions and the ratios between mean squared errors of the fits obtained in procedures B and A.

157 the length scale d_{eff} on which covariances decay exceeds the reach of direct connections by a large factor (Figure 3D). As the network approaches instability, which corresponds to the spectral bound R going to one, the
 158 effective decay constant diverges (Figure 3D inset) and so does the range of covariances.
 159

160 Our population-resolved theoretical analysis, furthermore, shows that the larger the spectral bound the more
 161 similar the decay constants between different populations, with only marginal differences for $R \lesssim 1$ (Figure 3E).
 162 This holds strictly if connection weights only depend on the type of the presynaptic neuron but not on the type
 163 of the postsynaptic neuron. Moreover, we find a relation between the squared effective decay constants and the
 164 squared anatomical decay constants of the form

$$d_{\text{eff},E}^2 - d_{\text{eff},I}^2 = \text{const.} \cdot (d_E^2 - d_I^2) \quad . \quad (2)$$

165 This relation is independent of the eigenvalues of the effective connectivity matrix, as the constant of order $\mathcal{O}(1)$
 166 does only depend on the choice of the connectivity profile. For $R \simeq 1$, this means that even though the absolute
 167 value of both effective length scales on the left hand side is large, their relative difference is small because it equals
 168 the small difference of anatomical length scales on the right hand side.

169 Pairwise covariances in motor cortex decay on a millimeter scale

170 To check if these predictions are confirmed by the data from macaque motor cortex, we first observe that, indeed,
 171 covariances in the resting state show a large dispersion over almost all distances on the Utah array (Figure 4).
 172 Moreover, the variance of covariances agrees well with the predicted exponential law: Performing an exponential
 173 fit reveals length constants above one millimeter. These large length constants have to be compared to the spatial
 174 reach of direct connections, which is about an order of magnitude shorter, in the range of $100 - 400 \mu\text{m}$ (20), so
 175 below the $400 \mu\text{m}$ inter-electrode distance of the Utah array. The shallow decay of the variance of covariances is,
 176 next to the broad distribution of covariances, a second indication that the network is in the dynamically balanced
 177 critical regime, in line with the prediction by Equation (1).

178 The population-resolved fits to the data show a larger length constant for excitatory covariances than for in-
179 hibitory ones (Figure 4A). This is qualitatively in line with the prediction of Equation (2) given the typically longer
180 reach of excitatory connections compared to inhibitory ones (34, 35). In the dynamically balanced critical regime,
181 however, the predicted difference in slope for all three fits is practically negligible. Therefore, we performed a
182 second fit where the slope of the three exponentials is constrained to be identical (Figure 4B). The error of this
183 fit is only marginally larger than the ones of fitting individual slopes (Figure 4C). This shows that differences in
184 slopes are hardly detectable given the empirical evidence, thus confirming the predictions of the theory given by
185 Equation (1) and Equation (2).

186 **Firing rates alter connectivity-dependent covariance patterns**

187 Since covariances measure the coordination of temporal fluctuations around the individual neurons' mean firing
188 rates, they are determined by how strong a neuron transmits such fluctuations from input to output (36). To leading
189 order this is explained by linear response theory (2, 33, 22, 21): How strongly a neuron reacts to a small change in
190 its input depends on its dynamical state, foremost the mean and variance of its total input, called "working point"
191 in the following. If a neuron receives almost no input, a small perturbation in the input will not be able to make
192 the neuron fire. If the neuron receives a large input, a small perturbation will not change the firing rate either,
193 as the neuron is already saturated. Only in the intermediate regime the neuron is susceptible to small deviations
194 of the input. Mathematically, this behavior is described by the gain of the neuron, which is the derivative of the
195 input-output relation (36). Due to the non-linearity of the input-output relation, the gain is vanishing for very small
196 and very large inputs and non-zero in the intermediate regime. How strongly a perturbation in the input to one
197 neuron affects one of the subsequent neurons therefore not only depends on the synaptic weight J but also on the
198 gain S and thereby the working point. This relation is captured by the effective connectivity $\mathbf{W} = \mathbf{S} \cdot \mathbf{J}$. What is
199 the consequence of the dynamical interaction among neurons depending on the working point? Can it be used to
200 reshape the low-dimensional manifold, the collective coordination between neurons?

201 The first part of this study finds that long-range coordination can be achieved in a network with short-range
202 random connections if effective connections are sufficiently strong. Alteration of the working point, for example
203 by a different external input, can affect the covariance structure: The pattern of coordination between individual
204 neurons can change, even though the anatomical connectivity remains the same. In this way, routing of information
205 through the network can be adapted dynamically on a mesoscopic scale. This is a crucial difference of such
206 coordination as opposed to coordination imprinted by complex but static connection patterns.

207 We first illustrate this concept by simulations of a network of nonlinear rate model neurons. For independent
208 and stationary external inputs covariances between neurons are solely generated inside the network via the recurrent
209 connectivity. External inputs only have an indirect impact on the covariance structure by setting the working point
210 of the neurons.

211 We create two networks with identical structural connectivity and identical external input fluctuations (Fig-
212 ure 5A). Small differences in mean external inputs between corresponding neurons in the two networks create
213 slightly different gains and firing rates and thereby differences in effective connectivity and covariances. Since
214 mean external inputs are drawn from the same distribution in both networks (Figure 5B), the overall distributions
215 of firing rates and covariances across all neurons are very similar (Figure 5E1,F2). But individual neurons' fir-
216 ing rates do differ (Figure 5E2). The resulting change of the neurons' working points substantially affects the
217 covariance patterns (Figure 5F2): Differences in firing rates and covariances between the two networks are sig-
218 nificantly larger than the differences within the same network across two different time periods (Figure 5C). The
219 larger the spectral bound, the more sensitive are the intrinsically generated covariances to the changes in firing
220 rates (Figure 5D). Thus, a small offset of individual firing rates is an effective parameter to control network-wide
221 coordination among neurons. As the input to the local network can be changed momentarily, we predict that in the
222 dynamically balanced critical regime coordination patterns should be highly dynamic.

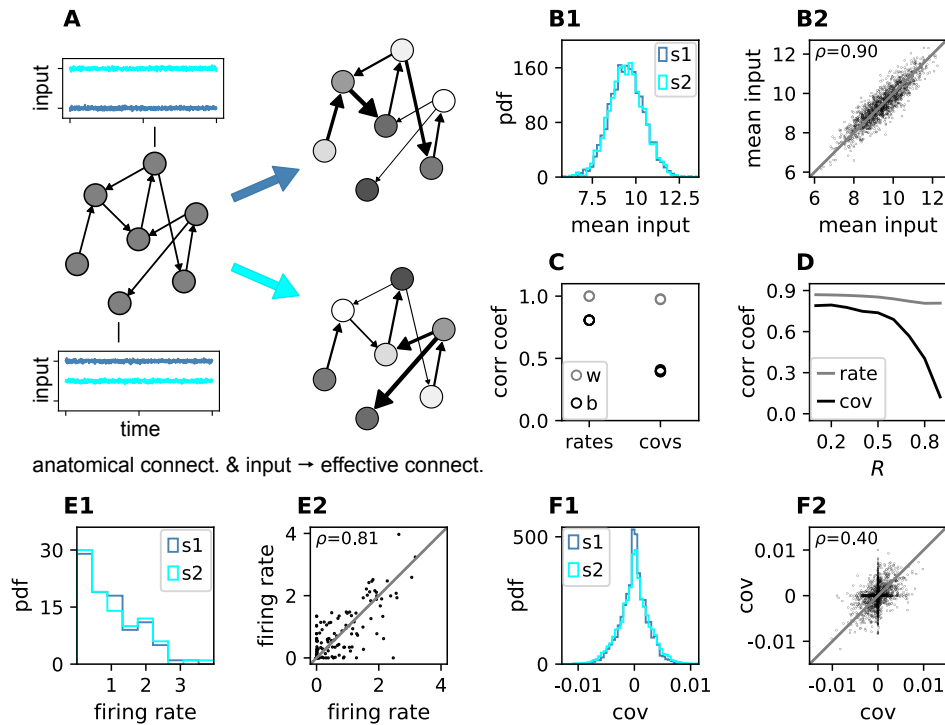


Figure 5: Changes in effective connectivity modify coordination patterns. (A) Two sparse random networks with identical structural connectivity (left network sketch) but different inputs (depicted by insets), which results in different firing rates (grayscale in right network sketches) and therefore different effective connectivities (thickness of connections). Parameters can be found in table T3 in the supplement. (B1) Histogram of input currents across neurons for the two networks (s1 and s2). (B2) Scatter plot of inputs to subset of 1500 corresponding neurons in the first and the second network. (C) Correlation coefficients of rates and of covariances between the networks (b, black) and within the same network (w, gray; simulation was split into two halves). (D) Correlation coefficient of rates (gray) and covariances (black) between the two networks as a function of the spectral bound R . (E1) Distribution of rates in the two networks (excluding silent neurons with $|\text{rate}| < 10^{-3}$). (E2) Scatter plot of rates in the first compared to the second network. (F1) Distribution of covariances in the two networks (excluding silent neurons). (F2) Scatter plot of sample of 5000 covariances in first compared to the second network. Other parameters: number of neurons $N = 2000$, connection probability $p = 0.1$, spectral bound for panels B, C, E, F is $R = 0.8$.

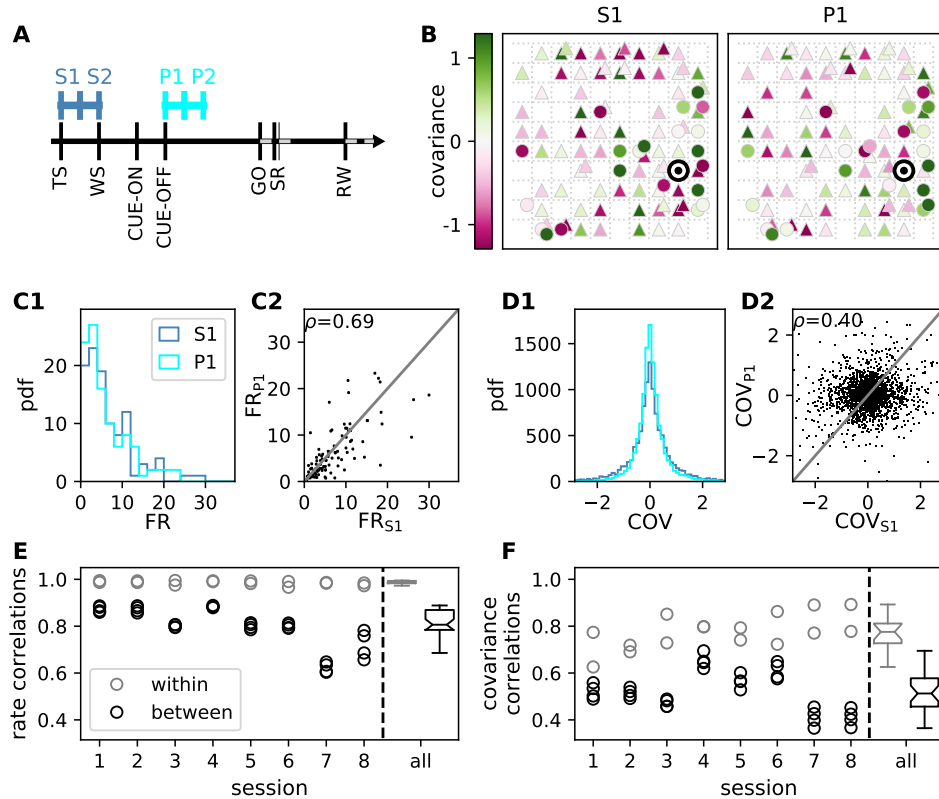


Figure 6: Behavioral condition reshapes mesoscopic neuronal coordination. (A) Trial structure of the reach-to-grasp experiment (37). Blue segments above the time axis indicate data pieces at trial start (dark blue: S1, S2) and during the preparatory period (light blue: P1, P2). (B) Salt-and-pepper structure of covariance during two different epochs (S1 and P1) of one recording session of monkey N (151 trials, 106 single units, cf. Figure 1 for recording setup). For some neurons the covariance completely reverses, while in the others it does not change. Inhibitory reference neuron indicated by black circle. (C1) Distributions of firing rates during S1 and P1. (C2) Scatter plot comparing firing rates in S1 and P1 (Pearson correlation coefficient $\rho = 0.69$). (D1/D2) Same as panels C1/C2, but for covariances (Pearson correlation coefficient $\rho = 0.40$). (E) Correlation coefficient of firing rates across neurons in different epochs of a trial for eight recorded sessions. Correlations between sub-periods of the same epoch (S1-S2, P1-P2; within-epoch, gray) and between sub-periods of different epochs (Sx-Py; between-epochs, black). Box plots to the right of the black dashed line show distributions obtained after pooling across all analyzed recording sessions per monkey. The line in the center of each box represents the median, box's area represents the interquartile range, and the whiskers indicate minimum and maximum of the distribution (outliers excluded). Those distributions differ significantly (Student t-test, two-sided, $p \ll 0.001$). (F) Correlation coefficient of covariances, analogous to panel e. The distributions of values pooled across sessions also differ significantly (Student t-test, two-sided, $p \ll 0.001$). For details of the statistical tests, see Methods. Details on number of trials and units in each recording session are provided in supplement S2.

223 **Coordination patterns in motor cortex depend on behavioral context**

224 In order to test the model prediction in experimental data, we analyze massively-parallel spiking activity from
225 macaque motor cortex, recorded during a reach-to-grasp experiment (37, 38). In contrast to the resting state, where
226 the animal was in an idling state, here the animal is involved in a complex task with periods of different cognitive
227 and behavioral conditions (Figure 6A). We compare two epochs in which the animal is requested to wait and is
228 sitting still but which differ in cognitive conditions. The first epoch is a starting period (S), where the monkey has
229 self-initiated the behavioral trial and is attentive because it is expecting a cue. The second epoch is a preparatory
230 period (P), where the animal has just received partial information about the upcoming trial and is waiting for
231 the missing information and the GO signal to initiate the movement. In both epochs the neuronal firing rates
232 are stationary, likely due to the absence of arm movement (see supplement S2). The overall distributions of the
233 firing rates in the different epochs are comparable (Figure 6C) but are distributed differently across the individual
234 neurons. By comparing the firing rates across neurons between disjoint sub-periods of any epoch (e.g. S1-S2 or
235 S1-P2), we observe that the firing rate compositions across neurons change more strongly across the two epochs
236 (Sx-Py) than within each of them (Figure 6E). This holds for data from five/eight different recording sessions from
237 different recording days for monkey E/N. Similarly, the covariance values change, though here the changes are
238 even more pronounced (Figure 6F). This is in line with our prediction for a network whose effective connectivity
239 has a large spectral bound, in the critically balanced state. In particular, the theory predicts different coordination
240 patterns between neurons on the mesoscopic scale (range of a Utah array), which is indeed observed in the two
241 states S and P (Figure 6B). The coordination between neurons is thus considerably reshaped by the behavioral
242 condition.

243 **Discussion**

244 In this study, we investigate coordination patterns of many neurons across mesoscopic distances in macaque mo-
245 tor cortex. We show that these patterns have a salt-and-pepper structure, which can be explained by a network
246 model with a spatially dependent random connectivity operating in a dynamically balanced critical state. In this
247 state, cross-covariances are shaped by a large number of parallel, multi-synaptic pathways, leading to interactions
248 reaching far beyond the range of direct connections. Strikingly, this coordination on the millimeter scale is only
249 visible if covariances are resolved on the level of individual neurons; the population mean of covariances quickly
250 decays with distance and is overall very small. In contrast, the variance of covariances is large and predominantly
251 decreases exponentially on length scales of up to several millimeters, even though direct connections typically only
252 reach a few hundred micrometers.

253 Since the observed coordination patterns are determined by the effective connectivity of the network, they are
254 dynamically controllable by the network state; for example, due to modulations of neuronal firing rates. Massively
255 parallel recordings in macaque motor cortex during resting state and in different epochs of a reach-to-grasp task
256 confirm this prediction. Simulations indeed exhibit a high sensitivity of coordination patterns to weak modulations
257 of the individual neurons' firing rates, providing a plausible mechanism for these dynamic changes.

258 Models of balanced networks have been investigated before (24, 39, 3, 21) and experimental evidence for cortical
259 networks operating in the balanced state is overwhelming (40, 41, 42). Excess of inhibition in such networks yields
260 stable and balanced population-averaged activities as well as low average covariances (21). Recently the notion
261 of balance has been combined with criticality in the dynamically balanced critical state that results from large
262 heterogeneity in the network connectivity (14). Here we focus on another ubiquitous property of cortical networks,
263 their spatial organization, and study the interplay between balance, criticality, and spatial connectivity in networks
264 of excitatory and inhibitory neurons. We show that in such networks, heterogeneity generates disperse covariance
265 structures between individual neurons on large length-scales with a salt-and-pepper structure.

266 Spatially organized balanced network models have been investigated before in the limit of infinite network
267 size, as well as under strong and potentially correlated external drive (5, 28). In this limit, intrinsically generated
268 covariances can be neglected and population-averaged covariances fulfill a linear equation, called the “balance

269 condition”, that predicts a non-monotonous change of population-averaged covariances with distance (43). In
270 contrast, we here consider covariances on the level of individual cells in finite-size networks with weak inputs or
271 in resting state conditions. In such a scenario, covariances have been shown to be predominantly generated locally
272 rather than from external inputs (4, 14). Analyses on the single-neuron level go beyond the balance condition and
273 require the use of field-theoretical techniques to capture the heterogeneity in the network (14).

274 The analysis performed here requires a theory for disordered systems with spatially non-homogeneous coupling
275 to analyze excitatory-inhibitory random networks on a two-dimensional sheet with spatially decaying connection
276 probabilities. This new theory allows us to derive expressions for the spatial decay of the variance of covariances.
277 We primarily evaluate these expressions in the long-range limit, which agrees well with simulations for distances
278 $x > 2d \sim \mathcal{O}(1 \text{ mm})$, which is fulfilled for most distances on the Utah array (cf. Figure 3, figure S4). For these
279 distances we find that the decay of covariances is dominated by a simple exponential law. Unexpectedly, its decay
280 constant is essentially determined by only two measures, the spectral bound of the effective connectivity, and the
281 length scale of direct connections. The length scale of covariances diverges when approaching the breakdown of
282 linear stability. In this regime, differences in covariances induced by differences in length scales of excitatory
283 and inhibitory connections become negligible. The predicted emergence of a single length scale of covariances is
284 consistent with our data.

285 This study focuses on local and isotropic connection profiles to show that long-range coordination does not
286 rely on specific connection patterns but can result from the network state alone. Alternative explanations for long-
287 range coordination are based on specifically imprinted network structures. Anisotropic local connection profiles
288 have been studied and shown to create spatio-temporal sequences (44) and long-range covariance patterns that
289 provide the seed for tuning maps in the visual cortex (45). Likewise, embedded excitatory feed-forward motifs and
290 cell assemblies via long-range patchy connections can create positive covariances at long distances (46, 47). These
291 structures are, however, imprinted in the connectivity: A change in gain of the neurons will either strengthen or
292 weaken the specific activity propagation, but it will not lead to new pathways of propagation within the network
293 and therefore not cause significantly different coordination patterns that we see in our data. The static impact of
294 these connectivity structures on covariances could in principle be included in the presented formalism. But, we
295 here show that heterogeneity through sparsity is enough to generate the dynamically balanced critical state, which
296 naturally provides a simple explanation for the broad distribution of covariances, the salt-and-pepper structure of
297 coordination, its long spatial range, and its sensitive dependence on the network state.

298 What are possible functional implications of the coordination on mesoscopic scales? Recent work demon-
299 strated activity in motor cortex to be organized in low-dimensional manifolds (6, 7, 8). Dimensionality reduction
300 techniques, such as PCA or GPFA (48), employ covariances to expose a dynamical repertoire of motor cortex
301 that is comprised of neuronal modes. Previous work started to analyze the relation between the dimensionality of
302 activity and connectivity (15, 16, 17, 14, 18, 19), but only in spatially unstructured networks, where each neuron can
303 potentially be connected to any other neuron. The majority of connections within cortical areas, however, stems
304 from local axonal arborizations (20). Here we add this biological constraint and demonstrate that these networks,
305 too, support a dynamically balanced critical state. This state in particular exhibits neural modes which are spanned
306 by neurons spread across the experimentally observed large distances. In this state a small subset of modes that are
307 close to the point of instability dominates the variability of the network activity and thus spans a low-dimensional
308 neuronal manifold. As opposed to specifically designed connectivity spectra via plasticity mechanisms (49) or
309 low-rank structures embedded into the connectivity (17), the dynamically balanced critical state is a mechanism
310 that only relies on the heterogeneity which is inherent to sparse connectivity and abundant across all brain areas.

311 While we here focus on covariance patterns in stationary activity periods, the majority of recent works studied
312 transient activity during motor behavior (6). How are stationary and transient activities related? During stationary
313 ongoing activity states, covariances are predominantly generated intrinsically (4). Changes in covariance patterns
314 therefore arise from changes in the effective connectivity via changes in neuronal gains, as demonstrated here in the
315 two periods of the reach-to-grasp experiment and in our simulations for networks close to criticality (Figure 5D).
316 During transient activity, on top of gain changes, correlated external inputs may directly drive specific neural modes
317 to create different motor outputs, thereby restricting the dynamics to certain subspaces of the manifold. In fact,

318 (50) reported that the covariance structures during movement preparation and movement execution are unrelated
319 and corresponding to orthogonal spaces within a larger manifold. Also (51) studied auditory and somatosensory
320 cortices of awake and anesthetized rats during spontaneous and stimulus-evoked conditions and found that neural
321 modes of stimulus-evoked activity lie in subspaces of the neural manifold spanned by the spontaneous activity.
322 Similarly, visual areas V1 and V2 seem to exploit distinct subspaces for processing and communication (52),
323 and motor cortex uses orthogonal subspaces capturing communication with somatosensory cortex or behavior-
324 generating dynamics (53). (7) further showed that manifolds are not identical, but to a large extent preserved
325 across different motor tasks due to a number of task-independent modes. This leads to the hypothesis that the
326 here described mechanism for long-range cooperation in the dynamically balanced critical state provides the basis
327 for low-dimensional activity by creating such spatially extended neural modes, whereas transient correlated inputs
328 lead to their differential activation for the respective target outputs. The spatial spread of the neural modes thereby
329 leads to a distributed representation of information that may be beneficial to integrate information into different
330 computations that take place in parallel at various locations. Further investigation of these hypotheses is an exciting
331 endeavor for the years to come.

332 **Methods**

333 **Experimental Design and Statistical Analysis**

334 Two adult macaque monkeys (monkey E - female, and monkey N - male) are recorded in behavioral experiments
335 of two types: resting state and reach-to-grasp. The recordings of neuronal activity in motor and pre-motor cortex
336 (hand/arm region) are performed with a chronically implanted $4 \times 4 \text{ mm}^2$ Utah array (Blackrock Microsystems).
337 Details on surgery, recordings, spike sorting and classification of behavioral states can be found in (38, 54, 37, 55).
338 All animal procedures were approved by the local ethical committee (C2EA 71; authorization A1/10/12) and
339 conformed to the European and French government regulations.

340 **Resting state data**

341 During the resting state experiment, the monkey is seated in a primate chair without any task or stimulation.
342 Registration of electrophysiological activity is synchronized with a video recording of the monkey's behavior.
343 Based on this, periods of "true resting state" (RS), defined as no movements and eyes open, are chosen for the
344 analysis. Eye movements and minor head movements are included. Each monkey is recorded twice, with a session
345 lasting approximately 15 and 20 min for monkeys E (sessions E1 and E2) and N (sessions N1 and N2), respectively,
346 and the behavior is classified by visual inspection with single second precision, resulting in 643 and 652 s of RS
347 data for monkey E and 493 and 502 s of RS data for monkey N.

348 **Reach-to-grasp data**

349 In the reach-to-grasp experiment, the monkeys are trained to perform an instructed delayed reach-to-grasp task
350 to obtain a reward. Trials are initiated by a monkey closing a switch (TS, trial start). After 400 ms a diode
351 is illuminated (WS, warning signal), followed by a cue after another 400 ms (CUE-ON), which provides partial
352 information about the upcoming trial. The cue lasts 300 ms and its removal (CUE-OFF) initiates a 1 s preparatory
353 period, followed by a second cue, which also serves as GO signal. Two epochs, divided into 200 ms sub-periods,
354 within such defined trials are chosen for analysis: the first 400 ms after TS (starting period, S1 and S2), and the
355 400 ms directly following CUE-OFF (preparatory period, P1 and P2) (cf. Figure 6a). Five selected sessions for
356 monkey E and eight for monkey N provide a total of 510 and 1111 correct trials, respectively. For detailed numbers
357 of trials and single units per recording session see supplement S2.

358 Separation of putative excitatory and inhibitory neurons

359 Offline spike-sorted single units (SUs) are separated into putative excitatory (broad-spiking) and putative inhibitory
360 (narrow-spiking) based on their spike waveform width (56, 57, 58, 59, 60). The width is defined as the time (num-
361 ber of data samples) between the trough and peak of the waveform. Widths of all average waveforms from all
362 selected sessions (both resting state and reach-to-grasp) per monkey are collected. Thresholds for “broadness”
363 and “narrowness” are chosen based on the monkey-specific distribution of widths, such that intermediate values
364 stay unclassified. For monkey E the thresholds are 0.33 ms and 0.34 ms, and for monkey N 0.40 ms and 0.41 ms.
365 Next, a two step classification is performed session by session. Firstly, the thresholds are applied to average SU
366 waveforms. Secondly, the thresholds are applied to SU single waveforms and a percentage of single waveforms
367 pre-classified as the same type as the average waveform is calculated. SU for which this percentage is high enough
368 are marked classified. All remaining SUs are grouped as unclassified. We verify the robustness of our results with
369 respect to changes in the spike sorting procedure in supplement S1.

370 Synchrofacts, i.e., spike-like synchronous events across multiple electrodes at the sampling resolution of the
371 recording system (1/30 ms) (61), are removed. In addition, only SUs with a signal-to-noise ratio (62) of at least
372 2.5 and a minimal average firing rate of 1 Hz are considered for the analysis, to ensure enough and clean data for
373 valid statistics.

374 Statistical analysis

375 All RS periods per resting state recording are concatenated and binned into 1 s bins. Next, pairwise covariances of
376 all pairs of SUs are calculated according to the following formula:

$$\text{COV}(i, j) = \frac{\langle b_i - \mu_i, b_j - \mu_j \rangle}{l - 1}, \quad (3)$$

377 with b_i, b_j - binned spike trains, μ_i, μ_j being their mean values, l the number of bins, and $\langle x, y \rangle$ the scalar product
378 of vectors x and y . Obtained values are broadly distributed, but low on average in every recorded session: in
379 session E1 E-E pairs: 0.19 ± 1.10 (M \pm SD), E-I: 0.24 ± 2.31 , I-I: 0.90 ± 4.19 , in session E2 E-E: 0.060 ± 1.332 ,
380 E-I 0.30 ± 2.35 , I-I 1.0 ± 4.5 , in session N1 E-E 0.24 ± 1.13 , E-I 0.66 ± 2.26 , I-I 2.4 ± 4.9 , in session N2 E-E
381 0.41 ± 1.47 , E-I 1.0 ± 3.1 , I-I 3.9 ± 7.3 .

382 To explore the dependence of covariance on the distance between the considered neurons, the obtained values
383 are grouped according to distances between electrodes on which the neurons are recorded. For each distance the
384 average and variance of the obtained distribution of cross-covariances is calculated. The variance is additionally
385 corrected for bias due to a finite number of measurements (14). In most of cases, the correction does not exceed
386 0.01%.

387 In the following step, exponential functions $y = a e^{-\frac{x}{d}}$ are fitted to the obtained distance-resolved variances
388 of cross-covariances (y corresponding to the variance and x to distance between neurons), which yields a pair
389 of values (a, d). The least squares method implemented in the Python `scipy.optimize` module (SciPy v.1.4.1) is
390 used. Firstly, three independent fits are performed to the data for excitatory-excitatory, excitatory-inhibitory, and
391 inhibitory-inhibitory pairs. Secondly, analogous fits are performed, with the constraint that the decay constant d
392 should be the same for all three curves.

Covariances in the reach-to-grasp data are calculated analogously but with different time resolution. For each
chosen sub-period of a trial, data are concatenated and binned into 200 ms bins, meaning that the number of spikes
in a single bin corresponds to a single trial. The mean of these counts normalized to the bin width gives the average
firing rate per SU and sub-period. The pairwise covariances are calculated according to Equation (3). To assess
the similarity of neuronal activity in different periods of a trial, Pearson product-moment correlation coefficients
are calculated on vectors of SU-resolved rates and pair-resolved covariances. Correlation coefficients from all
recording sessions per monkey are separated into two groups: using sub-periods of the same epoch (*within*-epoch),
and using sub-periods of different epochs of a trial (*between*-epochs). These groups are tested for differences with
significance level $\alpha = 0.05$. Firstly, to check if the assumptions for parametric tests are met, the normality of each

obtained distribution is assessed with a Shapiro-Wilk test, and the equality of variances with an F-test. Secondly, a t-test is applied to compare within- and between-epochs correlations of rates or covariances. Since there are two *within* and four *between* correlation values per recording session, the number of degrees of freedom equals: $df = (N_{\text{sessions}} \cdot 2 - 1) + (N_{\text{sessions}} \cdot 4 - 1)$, which is 28 for monkey E and 46 for monkey N. To estimate the confidence intervals for obtained differences, the mean difference between groups m and their pooled standard deviation s are calculated for each comparison

$$m = m_{\text{within}} - m_{\text{between}},$$

$$s = \sqrt{\frac{(N_{\text{within}} - 1)s_{\text{within}}^2 + (N_{\text{between}} - 1)s_{\text{between}}^2}{N_{\text{within}} + N_{\text{between}} - 2}},$$

393 with m_{within} and m_{between} being the mean, s_{within} and s_{between} the standard deviation and N_{within} and N_{between}
 394 the number of *within*- and *between*-epoch correlation coefficient values, respectively.

395 This results in 95% confidence intervals $m \pm t(df) \cdot s$ of 0.192 ± 0.093 for rates and 0.32 ± 0.14 for covariances
 396 in monkey E and 0.19 ± 0.14 for rates and 0.26 ± 0.17 for covariances in monkey N.

397 For both monkeys the *within*-epoch rate-correlations distribution does not fulfill the normality assumption of
 398 the t-test. We therefore perform an additional non-parametric Kolmogorov-Smirnov test for the rate comparison.
 399 The differences are again significant; for monkey E $D = 1.00, p = 6.66 \cdot 10^{-8}$; for monkey N $D = 1.00, p =$
 400 $8.87 \cdot 10^{-13}$.

401 For all tests we use the implementations from the Python `scipy.stats` module (SciPy v.1.4.1).

402 Mean and Variance of Covariances for a Two-Dimensional Network Model with Excita- 403 tory and Inhibitory Populations

404 The mean and variance of covariances are calculated for a two-dimensional network consisting of one excitatory
 405 and one inhibitory population of neurons. The connectivity profile $p(\mathbf{x})$, describing the probability of a neuron
 406 having a connection to another neuron at distance \mathbf{x} , decays with distance. We assume periodic boundary condi-
 407 tions and place the neurons on a regular grid (Figure 3A), which imposes translation and permutation symmetries
 408 that enable the derivation of closed-form solutions for the distance-dependent mean and variance of the covariance
 409 distribution. These simplifying assumptions are common practice and simulations show that they do not alter the
 410 results qualitatively.

Our aim is to find an expression for the mean and variance of covariances as functions of distance between two
 neurons. While the theory in (14) is restricted to homogeneous connections, understanding the spatial structure
 of covariances here requires us to take into account the spatial structure of connectivity. Field-theoretic methods
 allow us to obtain expressions for the mean covariance \bar{c} and variance of covariance $\overline{\delta c^2}$

$$\bar{c} = [\mathbf{1} - \mathbf{M}]^{-1} \frac{D}{1 - R^2} [\mathbf{1} - \mathbf{M}]^{-\text{T}}, \quad (4)$$

$$\overline{\delta c^2} = [\mathbf{1} - \mathbf{S}]^{-1} \left(\frac{D}{1 - R^2} \right)^2 [\mathbf{1} - \mathbf{S}]^{-\text{T}},$$

411 with identity matrix $\mathbf{1}$, mean \mathbf{M} and variance \mathbf{S} of connectivity matrix \mathbf{W} , input noise strength D , and spectral
 412 bound R . Since \mathbf{M} and \mathbf{S} have a similar structure, the mean and variance can be derived in the same way, which
 413 is why we only consider variances in the following.

414 To simplify Equation (4), we need to find a basis in which \mathbf{S} , and therefore also $\mathbf{A} = \mathbf{1} - \mathbf{S}$, is diagonal. Due
 415 to invariance under translation, the translation operators \mathbf{T} and the matrix \mathbf{S} have common eigenvectors, which
 416 can be derived using that translation operators satisfy $\mathbf{T}^N = \mathbf{1}$, where N is the number of lattice sites in x - or
 417 y -direction (see supplement). Projecting onto a basis of these eigenvectors shows that the eigenvalues $s_{\mathbf{k}}$ of \mathbf{S} are
 418 given by a discrete two-dimensional Fourier transform of the connectivity profile

$$s_{\mathbf{k}} \propto \sum_{\mathbf{x}} p(\mathbf{x}) e^{-i\mathbf{k}\mathbf{x}}.$$

419 Expressing A^{-1} in the eigenvector basis yields $A^{-1}(\mathbf{x}) = \mathbf{1} + B(\mathbf{x})$, where $B(\mathbf{x})$ is a discrete inverse Fourier
420 transform of the kernel $s_{\mathbf{k}}/(1 - s_{\mathbf{k}})$. Assuming a large network with respect to the connectivity profiles allows us
421 to take the continuum limit

$$B(\mathbf{x}) = \frac{1}{(2\pi)^2} \int d^2k \frac{s(\mathbf{k})}{1 - s(\mathbf{k})} e^{i\mathbf{k}\mathbf{x}} .$$

422 As we are only interested in the long-range behavior, which corresponds to $|\mathbf{x}| \rightarrow \infty$, or $|\mathbf{k}| \rightarrow 0$, respectively,
423 we can approximate the Fourier kernel around $|\mathbf{k}| \approx 0$ by a rational function, quadratic in the denominator, using
424 a Padé approximation. This allows us to calculate the integral which yields

$$B(\mathbf{x}) \propto K_0(-|\mathbf{x}|/d_{\text{eff}}) ,$$

425 where $K_0(x)$ denotes the modified Bessel function of second kind and zeroth order (63), and the effective decay
426 constant d_{eff} is given by Equation (1). In the long-range limit the modified Bessel function behaves like

$$B(\mathbf{x}) \underset{\infty}{\propto} \frac{\exp(-|\mathbf{x}|/d_{\text{eff}})}{\sqrt{|\mathbf{x}|}} .$$

427 Writing Equation (4) in terms of $B(\mathbf{x})$ gives

$$\overline{\delta c^2}(\mathbf{x}) = \left(\frac{D}{1 - R^2} \right)^2 [\delta(|\mathbf{x}|) + B(\mathbf{x}) + (B * B)(\mathbf{x})] ,$$

428 with the double asterisk denoting a two-dimensional convolution. $(B * B)(\mathbf{x})$ is a function proportional to the
429 modified Bessel function of second kind and first order (63), which has the long-range limit

$$(B * B)(\mathbf{x}) \underset{\infty}{\propto} \sqrt{|\mathbf{x}|} \exp(-|\mathbf{x}|/d_{\text{eff}}) .$$

430 Hence, the effective decay constant of the variances is given by d_{eff} . Note that further details of the above derivation
431 can be found in the supplement S3-S11.

432 Author contributions

433 A.R. and T.B. conducted the experiments. D.D., P.D., N.V., M.v.P. and S.G. analyzed the experimental data.
434 D.D., M.L., L.D. and M.H. developed the analytic theory. D.D., M.L., M.D. and M.H. designed the numerical
435 experiments. D.D., M.L., P.D., N.V., M.v.P., A.R., T.B., M.D., S.G. and M.H. wrote the manuscript.

436 Competing financial interests

437 The authors declare no competing financial interests.

438 Data availability

439 The data that support the findings of this study are available from the corresponding author upon reasonable request.

440

441 **Acknowledgments**

442 This work was partially supported by HGF young investigator's group VH-NG-1028, European Union's Horizon
443 2020 research and innovation program under Grant agreements No. 785907 (Human Brain Project SGA2) and
444 No. 945539 (Human Brain Project SGA3), ANR grant GRASP and partially funded by the Deutsche Forschungs-
445 gemeinschaft (DFG, German Research Foundation) - 368482240/GRK2416. We are grateful to our colleagues
446 in the NEST and Elephant developer communities and for continuous collaboration. All network simulations
447 were carried out with NEST 2.20.0 (<http://www.nest-simulator.org>). All data analyses performed with Elephant
448 (<https://neuralensemble.org/elephant/>). We thank Sebastian Lehmann for help with the design of the figures.

449 **References**

- 450 1. A. P. Georgopoulos, R. Caminiti, J. F. Kalaska, J. T. Massey, *Experimental Brain Research [Suppl.]* **7**, 327
451 (1983).
- 452 2. I. Ginzburg, H. Sompolinsky, *Phys. Rev. E* **50**, 3171 (1994).
- 453 3. A. Renart, *et al.*, *Science* **327**, 587 (2010).
- 454 4. M. Helias, T. Tetzlaff, M. Diesmann, *PLOS Comput. Biol.* **10**, e1003428 (2014).
- 455 5. R. Rosenbaum, B. Doiron, *Physical Review X* **4**, 021039 (2014).
- 456 6. J. A. Gallego, M. G. Perich, L. E. Miller, S. A. Solla, *Neuron* **94**, 978 (2017).
- 457 7. J. A. Gallego, *et al.*, *Nature Communications* **9**, 1 (2018).
- 458 8. J. A. Gallego, M. G. Perich, R. H. Chowdhury, S. A. Solla, L. E. Miller, *Nat. Neurosci.* **23**, 260 (2020).
- 459 9. D. Sussillo, M. M. Churchland, M. T. Kaufman, K. V. Shenoy, *Nat. Neurosci.* **18**, 1025 (2015).
- 460 10. L. F. Abbott, K. Rajan, H. Sompolinsky, *The Dynamic Brain: An Exploration of Neuronal Variability and its*
461 *Functional Significance* (2011), pp. 65–82.
- 462 11. L. Mazzucato, A. Fontanini, G. La Camera, *Frontiers in systems neuroscience* **10**, 11 (2016).
- 463 12. P. Gao, *et al.*, *bioRxiv* p. 214262 (2017).
- 464 13. C. Stringer, M. Pachitariu, N. Steinmetz, M. Carandini, K. D. Harris, *Nature* **571**, 361 (2019).
- 465 14. D. Dahmen, S. Grün, M. Diesmann, M. Helias, *Proc. Nat. Acad. Sci. USA* **116**, 13051 (2019).
- 466 15. J. Aljadeff, M. Stern, T. Sharpee, *Phys. Rev. Lett.* **114**, 088101 (2015).
- 467 16. J. Aljadeff, D. Renfrew, M. Veué, T. O. Sharpee, *Phys. Rev. E* **93**, 022302 (2016).
- 468 17. F. Mastrogiuseppe, S. Ostojic, *Neuron* **99**, 609 (2018).
- 469 18. D. Dahmen, *et al.*, *bioRxiv* (2020).
- 470 19. Y. Hu, H. Sompolinsky, *bioRxiv* (2020).
- 471 20. P. Schnepel, A. Kumar, M. Zohar, A. Aertsen, C. Boucsein, *Cerebral Cortex* **25**, 3818 (2015).

- 472 21. T. Tetzlaff, M. Helias, G. T. Einevoll, M. Diesmann, *PLOS Comput. Biol.* **8**, e1002596 (2012).
- 473 22. V. Pernice, B. Staude, S. Cardanobile, S. Rotter, *PLOS Comput. Biol.* **7**, e1002059 (2011).
- 474 23. V. Pernice, B. Staude, S. Cardanobile, S. Rotter, *Phys. Rev. E* **85**, 031916 (2012).
- 475 24. C. van Vreeswijk, H. Sompolinsky, *Science* **274**, 1724 (1996).
- 476 25. D. J. Amit, N. Brunel, *Cereb. Cortex* **7**, 237 (1997).
- 477 26. C. van Vreeswijk, H. Sompolinsky, *Neural Comput.* **10**, 1321 (1998).
- 478 27. R. Darshan, C. van Vreeswijk, D. Hansel **8**, 031072 (2018).
- 479 28. C. Baker, C. Ebsch, I. Lampl, R. Rosenbaum, *Phys. Rev. E* **99**, 052414 (2019).
- 480 29. J. Trousdale, Y. Hu, E. Shea-Brown, K. Josic, *PLOS Comput. Biol.* **8**, e1002408 (2012).
- 481 30. B. A. W. Brinkman, F. Rieke, E. Shea-Brown, M. A. Buice, *PLOS Comput. Biol.* **14**, e1006490 (2018).
- 482 31. R. Kobayashi, *et al.*, *Nature Communications* **10**, 1 (2019).
- 483 32. J. De la Rocha, B. Doiron, E. Shea-Brown, J. Kresimir, A. Reyes, *Nature* **448**, 802 (2007).
- 484 33. B. Lindner, B. Doiron, A. Longtin, *Phys. Rev. E* **72**, 061919 (2005).
- 485 34. M. W. Reimann, A.-L. Horlemann, S. Ramaswamy, E. B. Muller, H. Markram, *Cereb. Cortex* **27**, 4570 (2017).
- 486 35. Y. Hao, A. Riehle, T. G. Brochier, *Frontiers in neural circuits* **10**, 104 (2016).
- 487 36. M. Abeles, *Corticonics: Neural Circuits of the Cerebral Cortex* (Cambridge University Press, Cambridge,
488 1991), first edn.
- 489 37. T. Brochier, *et al.*, *Scientific Data* **5**, 180055 (2018).
- 490 38. A. Riehle, S. Wirtsohn, S. Grün, T. Brochier, *Frontiers in Neural Circuits* **7**, 48 (2013).
- 491 39. N. Brunel, *Journal of Computational Neuroscience* **8**, 183 (2000).
- 492 40. M. Okun, I. Lampl, *Nat. Neurosci.* **11**, 535 (2008).
- 493 41. K. Reinhold, A. D. Lien, M. Scanziani, *Nat. Neurosci.* **18**, 1789 (2015).
- 494 42. N. Dehghani, *et al.*, *Scientific Reports* **6** (2016).
- 495 43. R. Rosenbaum, M. A. Smith, A. Kohn, J. E. Rubin, B. Doiron, *Nat. Neurosci.* **20**, 107 (2017).
- 496 44. S. Spreizer, A. Aertsen, A. Kumar, *PLOS Comput. Biol.* **15**, e1007432 (2019).
- 497 45. G. B. Smith, B. Hein, D. E. Whitney, D. Fitzpatrick, M. Kaschube, *Nat. Neurosci.* **21**, 1600 (2018).
- 498 46. M. Diesmann, M.-O. Gewaltig, A. Aertsen, *Nature* **402**, 529 (1999).
- 499 47. A. Litwin-Kumar, B. Doiron, *Nat. Neurosci.* **15**, 1498 (2012).
- 500 48. B. M. Yu, *et al.*, *Journal of Neurophysiology* **102**, 614 (2009).
- 501 49. G. Hennequin, T. Vogels, W. Gerstner, *Neuron* **82**, 1394 (2014).

- 502 50. G. F. Elsayed, A. H. Lara, M. T. Kaufman, M. M. Churchland, J. P. Cunningham, *Nature Communications* **7**,
503 1 (2016).
- 504 51. A. Luczak, P. Barthó, K. D. Harris, *Neuron* **62**, 413 (2009).
- 505 52. J. D. Semedo, A. Zandvakili, C. K. Machens, M. Y. Byron, A. Kohn, *Neuron* **102**, 249 (2019).
- 506 53. M. G. Perich, *et al.*, *BioRxiv* (2020).
- 507 54. A. Riehle, T. Brochier, M. Nawrot, S. Grün, *Front. Neural Circuits* **12** (2018).
- 508 55. P. A. Dąbrowska, *et al.*, *bioRxiv* (2020).
- 509 56. P. Bartho, *et al.*, *J. Neurophysiol.* **92**, 600 (2004).
- 510 57. M. T. Kaufman, *et al.*, *Journal of Neurophysiology* **104**, 799 (2010).
- 511 58. M. T. Kaufman, M. M. Churchland, K. V. Shenoy, *Journal of Neurophysiology* **110**, 817 (2013).
- 512 59. A. Peyrache, *et al.*, *Proc. Nat. Acad. Sci. USA* **109**, 1731 (2012).
- 513 60. A. Peyrache, A. Destexhe, *Neurobiology of Disease* **130**, 104500 (2019).
- 514 61. E. Torre, *et al.* **36**, 8329 (2016).
- 515 62. N. Hatsopoulos, J. Joshi, J. G. O’Leary, *Journal of Neurophysiology* **92**, 1165 (2004).
- 516 63. F. W. J. Olver, D. W. Lozier, R. F. Boisvert, C. W. Clark, eds., *NIST Handbook of Mathematical Functions*
517 (Cambridge University Press, New York, NY, 2010).